

malization factor, a spatial smoothing parameter for slip velocity, and smoothness matrix (8). The log likelihood is approximately computed by adding  $\log[Z \int \exp[-(v_0 - \hat{v}_0)^T V_0^{-1} (v_0 - \hat{v}_0)] dv_0]$ , where  $\hat{v}_0$  and  $V_0$  are estimated  $v_0$  and its covariance in the first filtering, to logarithm of the above conditional probability with  $-\alpha^2 \hat{v}_0^T G \hat{v}_0$  in the second filtering, since  $Z \exp[-\alpha^2 \hat{v}_0^T G \hat{v}_0] \times$  (conditional probability)  $\propto \exp[-(v_0 - \hat{v}_0)^T V_0^{-1} (v_0 - \hat{v}_0)]$ .

10. P. Segall, M. Matthews, *J. Geophys. Res.* **102**, 22391 (1997).
11. J. J. McGuire, P. Segall, M. Miyazaki, *Eos* **82**, F265 (2001).
12. On the basis of Nishimura *et al.* (5), we estimate rectangular fault parameters of the Izu Islands model comprising dike, right-lateral and left-lateral faults (Fig. 4) by linear least squares fitting, using Okada's formula (22). Because of the sparsely distributed GPS sites in the Izu Islands compared with the Tokai region, we constrain the final state of the Izu Islands

model incorporating the estimated slip distribution on the above rectangular faults by Yabuki and Matsuura's method (23) to the total anomaly data for the entire period. We considered that the final state of the Izu Islands model is not so different from the solution by Yabuki and Matsuura's method. We also constrain that rake angle is within  $0 \pm 45$  for the right-lateral and left-lateral faults with unidirectional motion (17) over time for all the components including dike opening.

13. M. Ishida, *J. Geophys. Res.* **97**, 489 (1992).
14. S. Matsumura, *Tectonophysics* **273**, 271 (1997).
15. H. Hirose, K. Hirahara, F. Kimata, N. Fujii, S. Miyazaki, *Geophys. Res. Lett.* **26**, 3237 (1999).
16. I. Hirose, I. Kawasaki, Y. Okada, T. Sagiya, Y. Tamura, *J. Seismol. Soc. Jpn.* **53**, 11 (2000).
17. F. Kimata, K. Hirahara, N. Fujii, H. Hirose, *Eos* **82**, F266 (2001).
18. T. Sagiya, *Eos* **82**, F1265 (2001).
19. R. Harris, *J. Geophys. Res.* **103**, 24347 (1998).

20. A. T. Linde, I. S. Sacks, *Eos* **78**, F156 (1997).
21. Y. Fukahata, A. Nishitani, M. Matsuura, in preparation.
22. Y. Okada, Y., *Bull. Seismol. Soc. Am.* **75**, 1135 (1985).
23. T. Yabuki, M. Matsuura, *Geophys. J. Int.* **109**, 363 (1992).
24. We are grateful to S. Miyazaki of the Earthquake Research Institute, University of Tokyo, and J. J. McGuire and P. Segall of Stanford University for their explanation about their latest time-dependent inversion study.

#### Supporting Online Material

[www.sciencemag.org/cgi/content/full/1076780/DC1](http://www.sciencemag.org/cgi/content/full/1076780/DC1)  
Materials and Methods  
Figs. S1 and S2

30 July 2002; accepted 24 September 2002

Published online 3 October 2002;

10.1126/science.1076780

Include this information when citing this paper.

## Stronger Constraints on the Anthropogenic Indirect Aerosol Effect

Ulrike Lohmann\* and Glen Lesins

The anthropogenic indirect aerosol effects of modifying cloud albedo and cloud lifetime cannot be deduced from observations alone but require a modeling component. Here we validate a climate model, with and without indirect aerosol effects, by using satellite observations. The model agrees better with observations when both indirect aerosol effects are included. However, the simulated clouds are more susceptible to aerosols than the observed clouds from the POLDER satellite, thus overestimating the indirect aerosol effect. By taking the difference in susceptibilities into account, the global mean total anthropogenic aerosol effect is reduced from  $-1.4$  to  $-0.85$  watts per square meter.

The anthropogenic component of sulfate and carbonaceous aerosols has substantially increased the global mean aerosol burden from preindustrial times to the present and can influence climate in different ways. The direct aerosol effect is caused by the absorption and scattering of solar radiation. Additionally, aerosols exert an indirect effect by acting as cloud condensation nuclei, thereby affecting the initial cloud droplet number concentration (CDNC), albedo, precipitation formation, and lifetime of warm clouds. For a constant liquid water path, a higher cloud droplet number causes an increase in cloud albedo (cloud albedo effect). Reductions in precipitation efficiency due to more but smaller cloud droplets slow down precipitation formation and increase cloud lifetime (cloud lifetime effect). The cooling from both indirect effects has been estimated by climate models to be  $-1$  to  $-4.4$  W m $^{-2}$  in the global mean (1–5), but this estimate is still very

poorly constrained and is an important source of uncertainty in projections of future climate change (6, 7).

Data from a regional chemical transport model, together with satellite data estimating the cloud albedo effect in the North Atlantic, show that the cloud-top spherical albedo was enhanced over two-week episodes by 0.02 to 0.15 for the same liquid water path distribution (8) relative to the unperturbed case. POLDER satellite data were used (9) to derive aerosol concentration and cloud droplet effective radii (CDR) from 8 months of space-borne measurements and to explore the effect of aerosols on cloud microphysics. It was found that the cloud droplet size decreases with increasing aerosol index (AI) (10), which is representative of the aerosol column number concentration, indicating that the effect of aerosols on cloud microphysics is significant and occurs on a global scale. However, these data alone are not sufficient to quantify the magnitude of the global indirect aerosol effects between preindustrial times and present day.

From historical climate record data of oceanic and atmospheric warming together with ensembles of simulations with one

climate model of reduced complexity, the anthropogenic indirect aerosol effects have recently been constrained within the range of 0 to  $-1.2$  W m $^{-2}$  (11). Here, a complex global climate model rather than a simple climate model is used to try to determine the importance of the cloud albedo and the cloud lifetime effects by finding the model configurations that produce results that most resemble the observational data (9) in order to estimate the anthropogenic aerosol effects constrained by POLDER data.

We used the ECHAM4 general circulation model (GCM) (12) in T30 horizontal resolution to estimate the anthropogenic aerosol effect on a global scale. The GCM includes a fully coupled aerosol-cloud microphysics module (3, 13, 14). The reference simulation, ECHAM-CTL, includes both indirect aerosol effects with the use of present-day emissions (15). To turn off the cloud albedo effect (simulation ECHAM-2ND-AIE), we prescribed CDNC everywhere as a function of height in the radiation calculation: CDNC equals 150 cm $^{-3}$  near the surface and decreases to 50 cm $^{-3}$  in the midtroposphere. In the simulation ECHAM-NO-AIE, a constant number of cloud droplets was used in the cloud microphysics and the radiation calculations (16). We also ran a preindustrial climate simulation, ECHAM-PI, in which the sulfate and carbonaceous (black carbon and organic carbon) aerosols from fossil fuel and biomass burning were set to zero (17), leaving natural emissions from forests as the only source for organic carbon, and dimethyl sulfide emissions from the ocean and volcanoes as the only sources for sulfate aerosols.

Figure 1 shows AI as obtained from the control simulation as well as the difference between ECHAM's AI and that obtained from POLDER and averaged over March, April, and May 1997 (9, 18, 19). We calculated AI offline with the use of Mie theory, assuming an externally mixed aerosol (20). ECHAM correctly simulates a large land-sea contrast in AI, with the larger AI over land resulting from pollution as observed from

Department of Physics and Atmospheric Science, Dalhousie University, Halifax, Nova Scotia B3H 3J5, Canada.

\*To whom correspondence should be addressed. E-mail: Ulrike.Lohmann@Dal.Ca

## REPORTS

POLDER. ECHAM's AI agrees with that derived from POLDER over the oceans except for the transported Saharan dust. However, ECHAM largely underestimates AI over land, probably caused by too-large aerosol mode radii (21). The land-sea contrast in cloud droplet effective radius at the top of warm clouds, with cloud-top temperatures above 273.2 K and with smaller droplets over land, is also reproduced (22). However, ECHAM underestimates CDR, especially over continents of the Northern Hemisphere. Although ECHAM's liquid water path is in reasonable agreement with microwave observations (23), which are available only over oceans, its vertically integrated CDNC exceeds that derived from ISCCP satellite observations (24) in most parts of the world (not shown).

The question to be addressed is whether anthropogenic aerosol indirect effects are needed to explain the observed anticorrelation between AI and CDR, especially the larger negative slope over oceans, or whether these anticorrelations are determined purely by geographic variations in the liquid water path. ECHAM-CTL reproduces the observed anticorrelation between AI and CDR with a larger slope over oceans (Fig. 2). The slopes and linear correlation coefficients were computed over the same AI range (0 to 0.15) and covered the same geographical region between 60°N and 45°S as in (9). Whereas (9) used back trajectories to find the AI that belongs to a given CDR, we assumed that on a monthly basis AI and CDR can be taken from the same grid boxes in the model.

In the observations and in the model, the linear correlation coefficients between AI and CDR are  $-0.9$  over ocean and even higher over land. The larger oceanic slope, especially for low values of AI, is attributed to more susceptible clouds over the ocean. That is, for a similar AI over remote continental areas as over remote oceans, the continental cloud has a smaller liquid water path, leading to smaller CDR and thus smaller decreases of CDR with increasing AI, because AI values over land and ocean converge toward the same CDR limit in the POLDER data. A smaller CDR value is reached at high AI values for continental clouds in ECHAM, probably because of an overestimate in CDNC and an underestimated liquid water path in summer, when the continents tend to dry out.

The difference in cloud susceptibility over land and ocean is confirmed by the preindustrial simulation, ECHAM-PI. In this simulation, AI never exceeds 0.04 and, thus, the slope calculations are limited to that range. The oceanic clouds start with a higher CDR at the smallest AI but CDR rapidly decreases with increasing AI, whereas the CDR over land is almost constant with AI reflecting the

different distribution of liquid water path over land and ocean (Fig. 3).

If no indirect aerosol effect is taken into account as in ECHAM-NO-AIE, then the oceanic liquid water path decreases with increasing AI, thus increasing CDR for low AI and increasing its slope in worse agreement with observations. If only the cloud lifetime effect is considered as in ECHAM-2ND-AIE, then the difference in slope between oceanic and continental clouds increases, in better agreement with observations. Only the maritime clouds in ECHAM-NO-AIE show an anticorrelation between liquid water path and AI (Fig. 3). Again, the smallest absolute values in slope and correlation coefficient for oceanic

clouds in ECHAM-CTL are most in-line with recent findings from satellite data over oceans (25) showing no systematic trend of liquid water path on column aerosol number over the full range of column aerosol number concentration. Thus, we conclude that both aerosol indirect effects, including the more contentious cloud lifetime effect, are needed to reproduce the observed variation of CDR with AI and of AI with liquid water path.

Aerosol indirect effects exist even in the preindustrial simulation (Figs. 2 and 3). With increasing AI, the cloud droplet effective radius decreases and the liquid water path increases, especially in oceanic clouds. This finding complicates any attempt to detect an

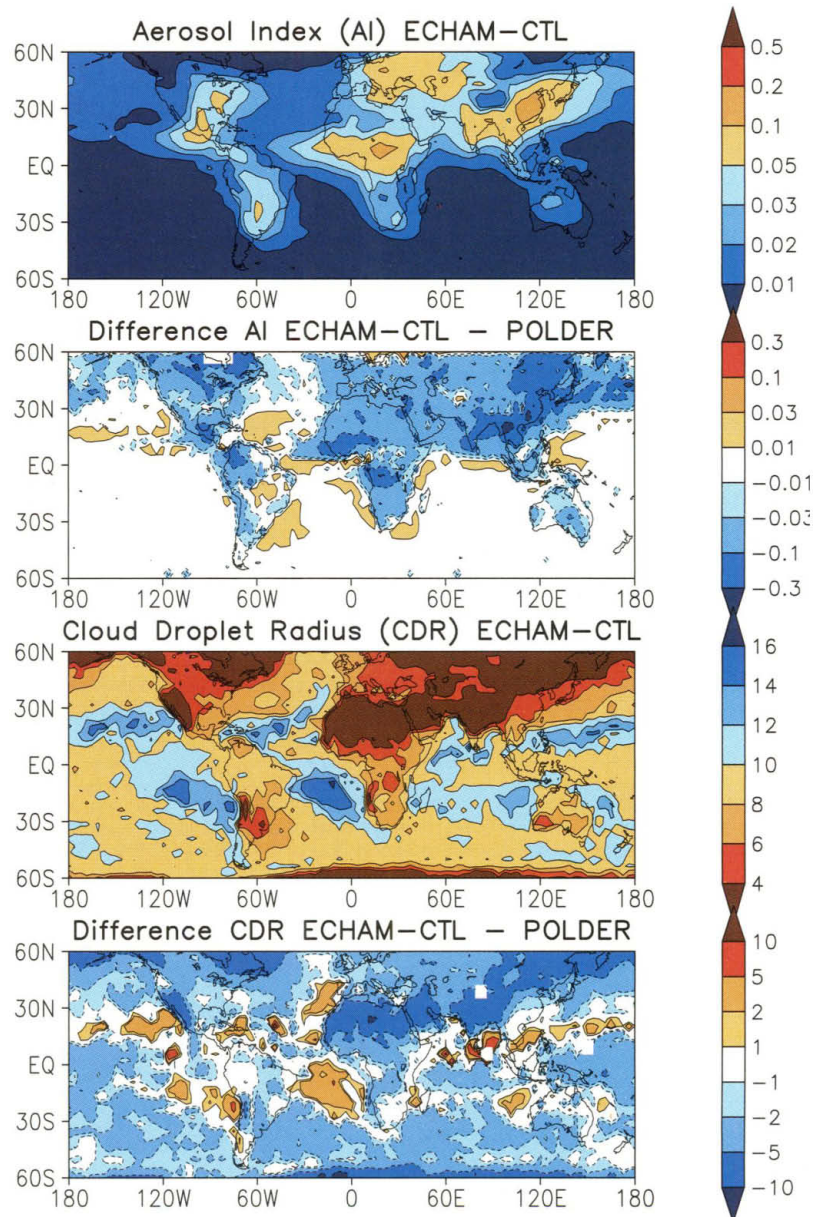


**Fig. 1.** AI and effective cloud droplet radius [in ( $\mu\text{m}$ ), indicated by color scale] averaged for March, April, and May 1997 from the ECHAM-CTL model simulation, and their differences between ECHAM-CTL and POLDER results.

anthropogenic aerosol indirect effect from observational data alone and demonstrates the importance of using models together with observations.

After showing evidence for the existence of both aerosol indirect effects, we used the climate model simulations including both indirect effects to estimate the global mean aerosol effects from preindustrial to present times. We obtain a decrease in shortwave radiation at the top of the

atmosphere of  $1.8 \text{ W m}^{-2}$ , which is accompanied by a  $0.4\text{-W m}^{-2}$  increase in long-wave radiation, such that the net radiation is reduced by  $1.4 \text{ W m}^{-2}$  in the global annual mean. However, the CDR-versus-AI plots showed that ECHAM's clouds are more susceptible to aerosols than the observed clouds, so ECHAM very likely overestimates the indirect aerosol effect. If CDR was constant with AI, then the indirect aerosol effect would be zero. Thus, we

use the difference in simulated versus observed slope over land and ocean to scale our estimate of the aerosol effect. ECHAM simulates an aerosol effect of  $-1.28 \text{ W m}^{-2}$  over oceans. Taking the factor of 1.3 in the overestimate in oceanic slope into account, the aerosol effect over oceans is reduced to  $-0.98 \text{ W m}^{-2}$ . Likewise, this method reduces the aerosol effect over land from  $-1.62$  to  $-0.53 \text{ W m}^{-2}$ , resulting in a net global mean aerosol effect of  $-0.85 \text{ W m}^{-2}$ . This new estimate of the net aerosol effects is consistent with the range of  $0$  to  $-1.2 \text{ W m}^{-2}$  estimated from historical climate record data coupled with a simple climate model for the indirect aerosol effects alone (11) and is much smaller than the purely model-based estimates (1, 2, 4).

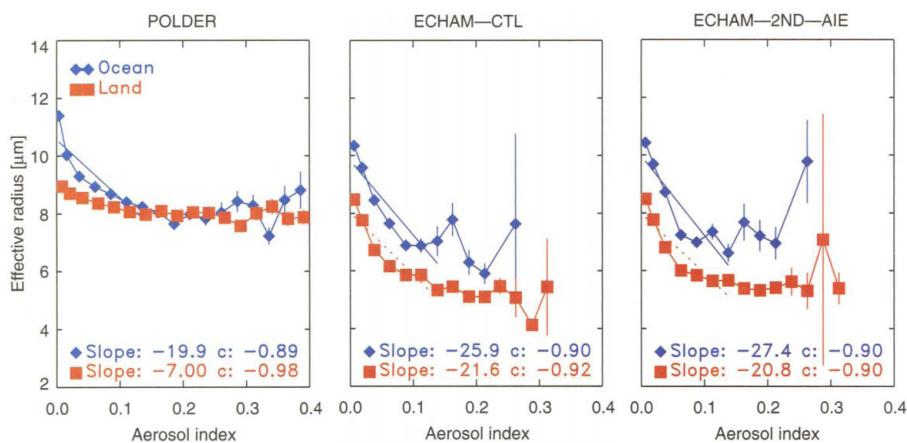


**Fig. 2.** Cloud droplet effective radius as a function of AI over oceans (diamonds) and over land (squares) from the POLDER satellite retrieval and ECHAM-CTL, ECHAM-2ND-AIE, ECHAM-NO-AIE, and ECHAM-PI model simulations. Straight lines are least-square fits for AI < 0.15. Error bars for observations and ECHAM refer to  $\pm 1$  standard error. The horizontal scale is reduced for ECHAM-PI.

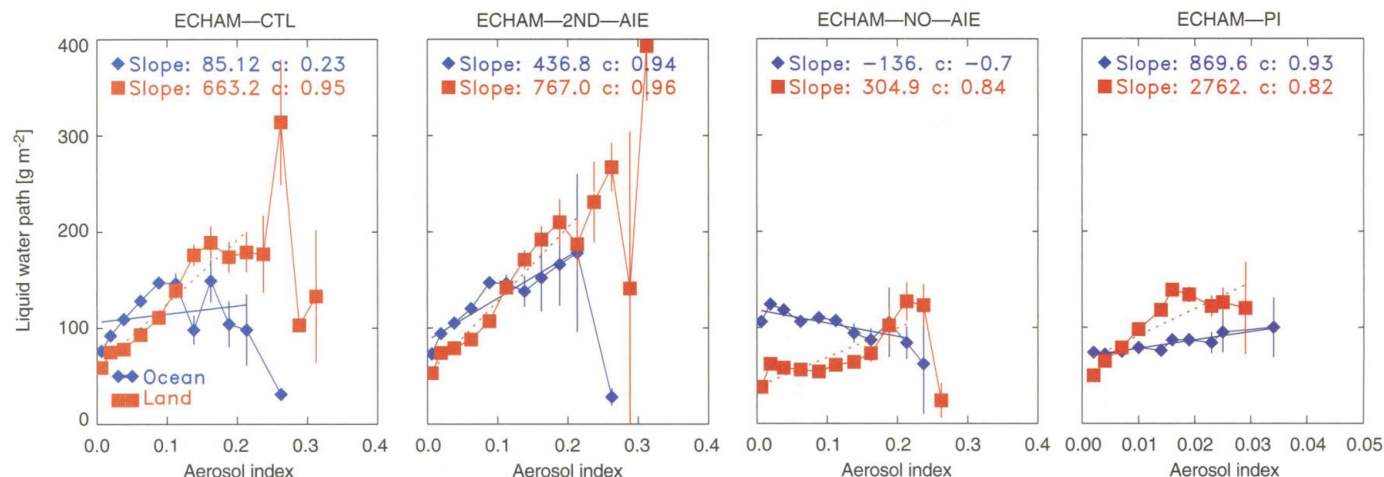
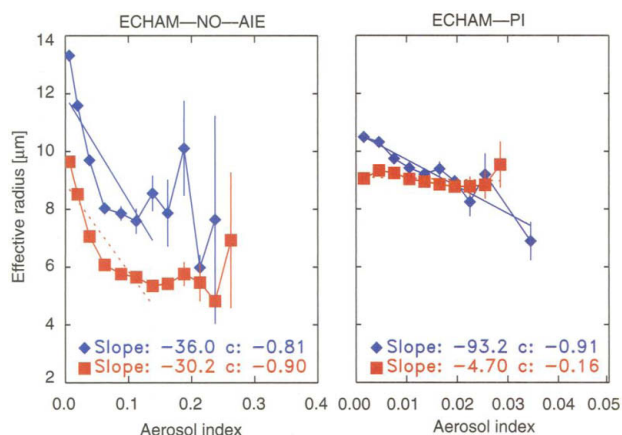


**Fig. 3.** Liquid water path as a function of AI over oceans (diamonds) and over land (squares) from the ECHAM-CTL, ECHAM-2ND-AIE, ECHAM-NO-AIE, and ECHAM-PI model simulations. The AI scale is different for ECHAM-PI.

References and Notes

1. S. J. Ghan *et al.*, *J. Geophys. Res.* **106**, 5279 (2001).
2. A. Jones, D. L. Roberts, M. J. Woodage, *J. Geophys. Res.* **106**, 20,293 (2001).
3. U. Lohmann, J. Feichter, *Geophys. Res. Lett.* **28**, 159 (2001).
4. L. D. Rotstain, *J. Geophys. Res.* **104**, 9369 (1999).
5. S. Menon, A. D. DelGenio, D. Koch, G. Tselioudis, *J. Atmos. Sci.* **59** (2002).
6. V. Ramaswamy *et al.*, *Climate Change 2001: The Scientific Basis. Contribution of Working Group I to the Third Assessment Report of the Intergovernmental Panel on Climate Change* (Cambridge Univ. Press, New York, 2001), pp. 349–416.
7. R. J. Charlson *et al.*, *Science* **292**, 2025 (2001).
8. S. E. Schwartz, Harshvardhan, C. Benkovitz, *Proc. Natl. Acad. Sci. U.S.A.* **99**, 1784 (2002).
9. F.-M. Bréon, D. Tanré, S. Generoso, *Science* **295**, 834 (2002).
10. The AI is defined as  $AI = 3.915 \tau_{865nm}$   

$$\ln \left( \frac{\tau_{670nm}}{\tau_{865nm}} \right)$$
11. R. Knutti, T. F. Stocker, F. Joos, G.-K. Plattner, *Nature* **416**, 719 (2002).
12. E. Roeckner *et al.*, *Tech. Rep.* **218**, Max (1996).
13. U. Lohmann, B. Kärcher, *J. Geophys. Res.* **107**, AAC8-1 (2002).
14. ECHAM4 solves prognostic equations for the mass mixing ratio of dimethyl sulfide, sulfur dioxide, sulfate aerosols, methane sulfonic acid, hydrophobic and hydrophilic organic and black carbon aerosols,

respectively, dust and sea salt aerosols; cloud liquid water and cloud ice mixing ratio; and number concentrations of cloud droplets and ice crystals. Transport, dry, and wet deposition, and chemical transformations of the aerosols and gaseous precursors are calculated online with the GCM. We used the auto-conversion rate of cloud droplets to form rain drops and the accretion rates of cloud droplets by (26).

15. The reference simulation ECHAM-CTL and the preindustrial climate simulation ECHAM-PI are 5-year integrations after an initial adjustment of 3 months, whereas the simulations with no aerosol indirect effects, ECHAM-NO-AIE, and cloud lifetime effect (second indirect effect) only, ECHAM-ZND-AIE, were integrated for 3 years after the initial 3-month adjustment.

16. It is not possible to only include the cloud albedo effect in a present-day simulation because if CDNC is constant in the cloud microphysics, then the precipitation

efficiency, the cloud lifetime, and the cloud liquid water path of water clouds change. This has a stronger implication for cloud radiative effects than expected from the cloud albedo effect alone. Furthermore, all simulations include aerosol direct effects.

17. There is no black carbon in the preindustrial simulation, and carbonaceous aerosol emissions from forest fires are neglected. Carbon dioxide levels are held constant at their present-day values.
18. F.-M. Bréon, S. Colzy, *Geophys. Res. Lett.* **27**, 4065 (2000).
19. J.-L. Deuzé *et al.*, *J. Geophys. Res.* **106**, 4913 (2001).
20. M. Hess, P. Koepke, I. Schult, *Bull. Am. Meteorol. Soc.*, **79**, 831 (1998).
21. G. Lesins, U. Lohmann, in preparation.
22. More and smaller cloud droplets over land are caused by more vigorous updrafts and more aerosol particles.

23. T. J. Greenwald, G. L. Stephens, T. H. Vonder Haar, D. L. Jackson, *J. Geophys. Res.* **98**, 18,471 (1993).
24. Q. Han, W. B. Rossow, J. Chou, R. Welch, *Geophys. Res. Lett.* **25**, 1419 (1998).
25. T. Nakajima, A. Higurachi, K. Kawamoto, J. E. Penner, *Geophys. Res. Lett.* **28**, 1171 (2001).
26. M. Khairoutdinov, Y. Kogan, *Mon. Weather Rev.* **128**, 229 (2000).
27. We thank F.-M. Bréon for providing the POLDER data and S. Ghan and one anonymous reviewer for helpful comments and suggestions. Supported by the National Science and Engineering Research Council of Canada and the Canadian Foundation for Climate and Atmospheric Science collaborative research grants. We thank the Deutsches Klimarechenzentrum for computing time.

21 June 2002; accepted 24 September 2002

## Climate Change and Latitudinal Patterns of Intertidal Thermal Stress

Brian Helmuth,<sup>1\*</sup> Christopher D. G. Harley,<sup>2,3</sup> Patricia M. Halpin,<sup>4,6</sup> Michael O'Donnell,<sup>3</sup> Gretchen E. Hofmann,<sup>5,6</sup> Carol A. Blanchette<sup>6</sup>

The interaction of climate and the timing of low tides along the West Coast of the United States creates a complex mosaic of thermal environments, in which northern sites can be more thermally stressful than southern sites. Thus, climate change may not lead to a poleward shift in the distribution of intertidal organisms, as has been proposed, but instead will likely cause localized extinctions at a series of "hot spots." Patterns of exposure to extreme climatic conditions are temporally variable, and tidal predictions suggest that in the next 3 to 5 years "hot spots" are likely to appear at several northern sites.

A central goal in exploring the consequences of global climate change is to accurately predict the alteration of thermal stresses on organisms and the subsequent impact of stress on the distribution patterns of species. Specifically, the prediction that species distributions will shift poleward as global warming continues depends on the idea that thermal stresses are always higher at their more-equatorial ends. Because they are assumed to live very close to their thermal tolerance limits (1–4), organisms inhabiting the rocky intertidal zone have emerged in recent years as potential harbingers of the effects of climate change on species distributional patterns in nature (3–9). To explore these patterns, scientists working in coastal environments typically rely on air and water tempera-

tures as proxies for body temperatures (5–10). Although this approach is appropriate for subtidal organisms (10), the body temperatures of intertidal organisms during aerial exposure at low tide are, in contrast, driven by multiple climatic factors, and can be very different from air or water temperatures (11–18). Furthermore, the mechanics of heat flux depend to a large extent on organism morphology, material properties, and color; thus, two organisms exposed to identical climatic conditions can display very different body temperatures (11–16). Lastly, whereas the temperatures of intertidal organisms are driven by terrestrial climatic factors, the timing of the alternating exposure to terrestrial and marine environments is driven by the dynamics of the tidal cycle. However, despite the observation that body temperatures are often much higher during aerial exposure at low tide than during immersion (15–18), and although (in temperate regions) thermal damage of proteins occurs at temperatures almost exclusively experienced during aerial exposure (19–22), most studies to date have focused only on geographic patterns of water temperature in setting the distribution of intertidal species (5–10, 23). Under such a model, climate change is predicted to cause a poleward shift in species

distributions as temperatures at the equatorial end surpass the physiological tolerances of the species in question (3, 6, 7).

We explore how thermal stress in rocky intertidal habitats varies along a latitudinal gradient, and we provide evidence that body temperatures do not increase monotonically with decreasing latitude. We focus on the intertidal mussel *Mytilus californianus*, an abundant and widely distributed species that is a competitive dominant in the intertidal ecosystem (24); however, the issues that we describe apply to all intertidal species (16). We deployed a series of temperature loggers modified to thermally match living mussels (25) in mussel beds (26) at eight sites spanning 14° of latitude ranging from northern Washington to Point Conception, California (27). Sites were not chosen at random or at fixed intervals; instead, we selected locations where previous intertidal studies have been conducted (17, 19–21, 24, 28–31) in an effort to place these sites in a comparative framework with one another with regard to thermal stress.

Data from each instrument were summarized using two temperature metrics. The 99th percentile of all temperatures recorded from May to September at each site was calculated as the summer maximum, a measure of "acute" stress (17, 32). The average daily maximum [(ADM), the average of all daily peaks] was also calculated for each month as a measure of "chronic" high-temperature exposure (17), and the highest monthly value of ADM for each site was considered as the peak ADM. Data were analyzed using a Kruskal-Wallis test (Statview), which was used to rank sites in descending order from "hottest" to "coolest" for comparison with the null model of monotonically increasing thermal stress with decreasing latitude (33).

Results clearly indicated that body temperatures did not become more thermally stressful with decreasing latitude, and that the patterns of stress varied to some extent with the temperature metric in question (Fig. 1). There was no clear latitudinal pattern in either of the temperature metrics. Whereas conditions were slightly hotter at Jalama and Alegria, California, two wave-protected sites near Point Conception (Fig. 1), Boiler Bay and Strawberry Hill, Ore-

<sup>1</sup>University of South Carolina, Department of Biological Sciences and Marine Sciences Program, Columbia, SC 29208, USA. <sup>2</sup>University of Washington, Department of Zoology, Box 351800, Seattle, WA 98195, USA. <sup>3</sup>Stanford University, Hopkins Marine Station, Pacific Grove, CA 93950, USA. <sup>4</sup>Oregon State University, Department of Zoology, Corvallis, OR 97331, USA. <sup>5</sup>Department of Ecology, Evolution and Marine Biology. <sup>6</sup>Marine Science Institute, University of California, Santa Barbara, CA 93106, USA.

\*To whom correspondence should be addressed. E-mail: helmuth@biol.sc.edu